

Article

Novel Bi₃O₅I₂ Hollow Microsphere and Its Enhanced Photocatalytic Activity

Baoyin Cui ^{1,2}, Haitao Cui ¹, Zhenrong Li ¹, Hongyu Dong ¹, Xin Li ¹, Liangfu Zhao ^{1,*} and Junwei Wang ¹

¹ Institute of Coal Chemistry, Chinese Academy of Sciences, Taiyuan 030001, China

² University of the Chinese Academy of Sciences, Beijing 100049, China

* Correspondence: lzfzhao@sxicc.ac.cn; Tel.: +86-1348-536-2851

Received: 29 July 2019; Accepted: 22 August 2019; Published: 24 August 2019



Abstract: A new type of I-deficient bismuth oxyiodide Bi₃O₅I₂ with a hollow morphology was prepared by the solvothermal process. The structure, composition, morphology, optical property and photoelectric property of the as prepared photocatalyst were investigated through some characterization methods. Those characterization results showed that Bi₃O₅I₂ displayed a larger specific surface area, promising band structure and lower recombination of photoinduced carriers than pure BiOI. Bi₃O₅I₂ had a higher photocatalytic activity than BiOI on the decomposition of methyl orange (MO) under simulated solar light irradiation. The superoxide ($\cdot\text{O}_2^-$) and hole (h^+) were the dominating active species during the degradation of MO. Its stability and reusability performance showed its great promising application in the degradation of organic pollutant.

Keywords: Bi₃O₅I₂; BiOI; hollow structure; photocatalysts; MO degradation

1. Introduction

With increasing concerns on environmentally friendly processes, semiconductor photocatalysts have been given widely attention because of their promising applications. Among the multitudinous semiconductor photocatalysts, bismuth oxyiodide (BiOI) with unique layered crystal configuration [1–3] and excellent visible light absorption [4,5], is a promising photocatalytic material in the field of energy and environment [6–10]. Nevertheless, the photocatalytic activity of bismuth oxyiodide is far from potential industrial applications because of their relatively high recombination of photogenerated carriers and insufficient reduction and oxidation ability [11,12]. For the sake of increasing the photocatalytic performance of BiOI, measures should be taken to decrease the recombination of photogenerated carriers and improving its reduction and oxidation ability. So far, many measures have been taken to enhance the photocatalytic performance of BiOI, such as regulating morphology [13–16], exposing special crystal face [17–19], doping [20–23], compositing with other semiconductor [24–27] and synthesizing other bismuth oxyiodides such as Bi₄O₅I₂ [12,28], Bi₅O₇I [29–31] and Bi₇O₉I₃ [32,33].

Aside from BiOI, I-deficient bismuth oxyiodides have the positive oxidation and reduction ability [11,12], leading to its high photocatalytic activity. For example, Zhang et al. discovered that Bi₄O₅I₂ and Bi₅O₇I displayed enhanced photocatalytic activity for degradation of tetracycline hydrochloride, bisphenol A and Rhodamine B [11]. Ye et al. synthesized Bi₄O₅I₂ photocatalyst with excellent activities for photocatalytic H₂ evolution [12]. Generally, I-deficient bismuth oxyiodides were prepared by four methods: (1) Hydrothermal progress using the pH modifier [34], (2) in situ calcination progress of BiOI [11], (3) hydrolytic process of the bismuth molecular precursor [12], (4) chemical etching method for bismuth oxides [35]. However, these methods were time consuming or introduce potential environmental and safety problems. Therefore, a simple method of synthesizing the I-deficient bismuth oxyiodide is needed.

It is generally accepted that the morphology of the catalysts has the close relation with the catalyst performance [36,37]. Photocatalysts with a hollow structure display excellent photocatalytic performance on account of their high specific surface area. In addition, both their high energy conversion efficiencies and their strong light-harvesting capacities contribute to their excellent photocatalytic performance [15,38,39]. For example, Li et al. found that BiOI with hollow structures presented a higher photocatalytic performance than those BiOI with low-dimensional [15]. Until now, the I-deficient bismuth oxyiodide with different morphologies are synthesized by several researchers, including sheet-like morphology [40], rod-like morphology [29] and flower-like morphology [33,41]. However, there are no reports about synthesizing the I-deficient bismuth oxyiodide with hollow structure. Therefore, a hollow structure of the I-deficient bismuth oxyiodide should be synthesized.

In this research, a new type of I-deficient bismuth oxyiodide with a hollow structure was prepared by the hydrothermal progress for the first time. Their structures as well as its photocatalytic ability for the demineralization of methyl orange (MO) were discussed under systematical characterization.

2. Results

2.1. Molecular Formula Characterization and Phase Transformation

The energy dispersive spectrometry (EDS) apparatus was employed to investigate the chemical composition on the surface of the as prepared I-deficient bismuth oxyiodide. As shown in Figure 1, the I-deficient bismuth oxyiodide contained Bi, O and I elements. Meanwhile, the associated EDS elemental maps confirmed that these elements were distributed homogeneously. As shown in Table S1, the average Bi:O:I ratio in the surface of the I-deficient bismuth oxyiodide was 3:4.7:2, in conformity with the molecular formula $\text{Bi}_3\text{O}_5\text{I}_2$ (3:5:2). This result indicated that its chemical composition possibly was $\text{Bi}_3\text{O}_5\text{I}_2$. Meanwhile, the average Bi:O:I ratio of the pure BiOI are 1:1.1:1 (Table S2), which is close to the ideal ratio for BiOI (1:1:1). This indicated that the result of the EDS was convincing.

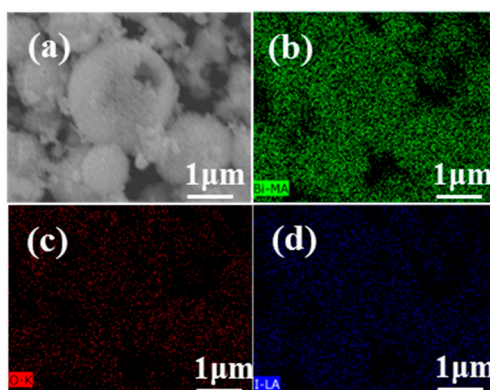


Figure 1. The SEM image of the I-deficient bismuth oxyiodide (a) and Bi, O, I elemental maps of I-deficient bismuth oxyiodide (b–d).

The inductively coupled plasma (ICP) analysis showed that the percentage of the Bi element in the bulk bismuth oxyiodide was 64.95%, in conformity with the molecular formula $\text{Bi}_3\text{O}_5\text{I}_2$ (65%). Consequently, based on the analysis of ICP and EDS, the molecular formula of the as prepared I-deficient BiOI can possibly be determined as $\text{Bi}_3\text{O}_5\text{I}_2$. Therefore, the I-deficient bismuth oxyiodide was labelled as $\text{Bi}_3\text{O}_5\text{I}_2$ in the following.

A thermogravimetric (TG) measurement was carried out to evaluate the phase transformation of $\text{Bi}_3\text{O}_5\text{I}_2$ and BiOI and the result was shown in Figure 2. In Figure 2, the TG curve of the $\text{Bi}_3\text{O}_5\text{I}_2$ sample was composed by three mass loss steps. The first mass loss step (250–360 °C) was attributed to the transformation from $\text{Bi}_3\text{O}_5\text{I}_2$ to $\text{Bi}_4\text{O}_5\text{I}_2$, whereas the second mass loss step (400–520 °C) was ascribed to the transformation from $\text{Bi}_4\text{O}_5\text{I}_2$ to $\text{Bi}_5\text{O}_7\text{I}$, the third step (580–760 °C) was ascribed to the transformation from $\text{Bi}_5\text{O}_7\text{I}$ to Bi_2O_3 , which can be illustrated as Equation (1). The weight remaining

of each phase transformation step in Equation (1) was calculated to be 91.3%, 80.2% and 73.8%, respectively, which is very similar to the experimental value (91.7%, 80.1% and 73.2%). This result shows that the molecular formula $\text{Bi}_3\text{O}_5\text{I}_2$ is correct. According to the results of EDX, ICP and TG, the as prepared I-deficient bismuth oxyiodide can be determined as $\text{Bi}_3\text{O}_5\text{I}_2$. The phase transformation of BiOI

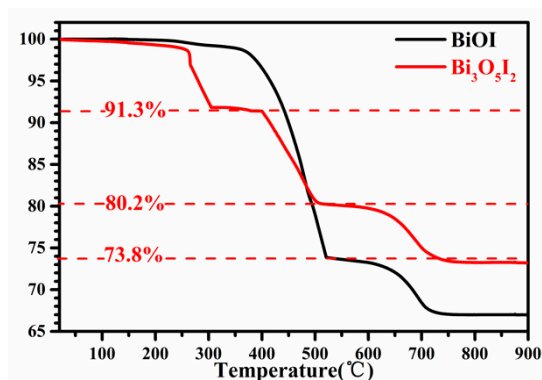
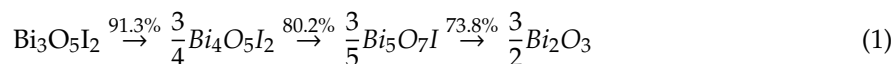


Figure 2. Thermogravimetric (TG) profiles of $\text{Bi}_3\text{O}_5\text{I}_2$ and bismuth oxyiodide (BiOI) samples in air flow.

2.2. Structure Investigation and Morphology Observation

The crystal information of $\text{Bi}_3\text{O}_5\text{I}_2$ and BiOI were characterized by the X-ray diffraction (XRD), which was shown in Figure 3. The main diffraction peaks of the as prepared $\text{Bi}_3\text{O}_5\text{I}_2$ (Figure 3a) could be clearly seen at 2θ of 10.1° , 20.5° , 29.2° , 31.7° , 45.7° , 52.6° , 55.1° and 64.3° , respectively. According to the JCPDS file 73–2062, the diffraction peaks at 9.7° , 29.3° , 31.9° , 45.4° , 51.5° and 55.4° are corresponding to the (001), (012), (110), (020), (114) and (122) of BiOI, respectively, which is different with the main diffraction peaks of the as prepared $\text{Bi}_3\text{O}_5\text{I}_2$.

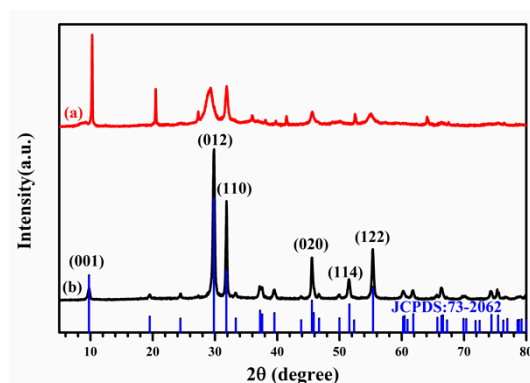


Figure 3. The XRD patterns of: (a) $\text{Bi}_3\text{O}_5\text{I}_2$; (b) BiOI.

The typical scanning electron microscope (SEM) and transmission electron microscopy (TEM) were shown in Figure 4. It was clearly seen that $\text{Bi}_3\text{O}_5\text{I}_2$ had a hollow microsphere morphology with an average diameter of 1–3 μm and the entire sphere like structures were composed of numerous nanoplates (Figure 4a,b). In Figure 4c, there were clearly a contrast between the dark boundary and the relatively bright center, which further confirmed their hollow nature [42]. In Figure 4d, clear lattice fringes showed that the lattice spacing were 0.312 nm and 0.339 nm, which might be the (102) and (101) plane of $\text{Bi}_3\text{O}_5\text{I}_2$.

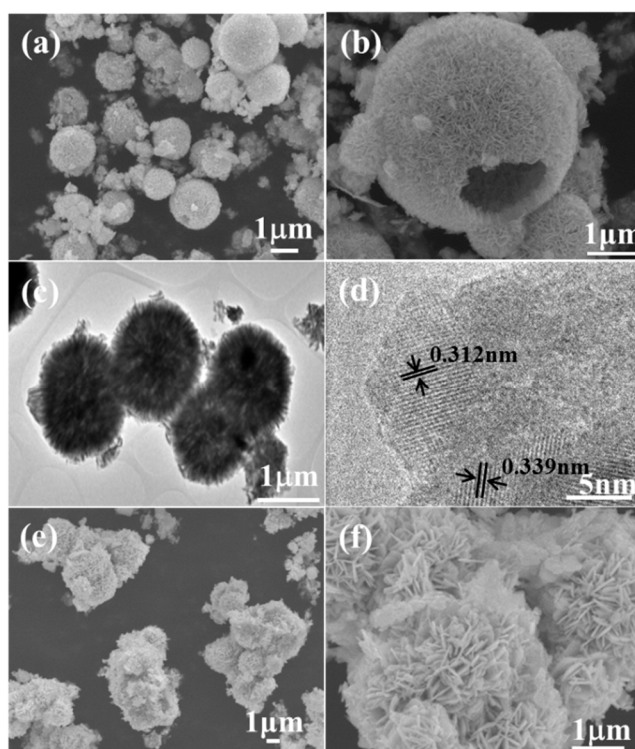


Figure 4. (a,b) SEM image of $\text{Bi}_3\text{O}_5\text{I}_2$; (c,d) TEM image of $\text{Bi}_3\text{O}_5\text{I}_2$; (e,f) SEM image of BiOI.

The surface chemical compositions of the $\text{Bi}_3\text{O}_5\text{I}_2$ and the pure BiOI, as well as the chemical states of them, were investigated by the X-ray photoelectron spectroscopy (XPS), which was shown in Figure 5. In Figure 5a, it could be seen that the surfaces of $\text{Bi}_3\text{O}_5\text{I}_2$ and BiOI consisted of Bi, O, I and C elements (C may come from the reference sample), indicating a high purity of $\text{Bi}_3\text{O}_5\text{I}_2$ and BiOI. In Figure 5b, the binding energy values of the Bi 4f spectrum of the BiOI was about 158.6 eV and 163.9 eV, which correspond to Bi 4f_{7/2} and Bi 4f_{5/2}. It indicated the presence of Bi³⁺ in the sample [43]. As for the $\text{Bi}_3\text{O}_5\text{I}_2$, the peak of Bi 4f_{7/2} (or 4f_{5/2}) peak could be decomposed into two bimodal peaks of 158.5 eV and 159.2 eV (or 163.8 eV and 164.5 eV), which could be ascribed to Bi³⁺ and Bi⁵⁺, respectively [44]. The O 1s spectrum of BiOI (presented in Figure 5c) had two peaks. One was at 530.8 eV and the other was at 532.9 eV. The peak at 530.8 eV should be attributed to the Bi-O bonds the existed in BiOI. The peak at 532.9 eV should be attributed to the O-H bonds on the surface of BiOI [43]. The O 1s spectrum of $\text{Bi}_3\text{O}_5\text{I}_2$ had three peaks at 530.7 eV, 531.4 eV and 532.9 eV. The peak at 530.7 eV belongs to the Bi³⁺-O bonds in the $\text{Bi}_3\text{O}_5\text{I}_2$ lattice [45]. The peak at 531.4 eV belongs to the Bi⁵⁺-O bonds in the $\text{Bi}_3\text{O}_5\text{I}_2$ lattice [43]. In addition, the peak at 532.9 eV belongs to the O-H bonds that existed on the $\text{Bi}_3\text{O}_5\text{I}_2$ surface. As shown in Figure 5d, the two peaks can be observed at 630.1 eV and 618.6 eV. They were ascribed to I 3d_{5/2} and I 3d_{3/2}, which could be assigned to the monovalent oxidation state of the I elements in BiOI [43]. It should be noted that the peaks for I 3d of the $\text{Bi}_3\text{O}_5\text{I}_2$ samples (630.4 eV and 618.9 eV) presented a 0.3 eV shift to higher binding energy. This implied that the I in $\text{Bi}_3\text{O}_5\text{I}_2$ possibly existed at a different ambient chemical environment [43]. The XPS character showed that the Bi in the $\text{Bi}_3\text{O}_5\text{I}_2$ includes Bi³⁺ and Bi⁵⁺.

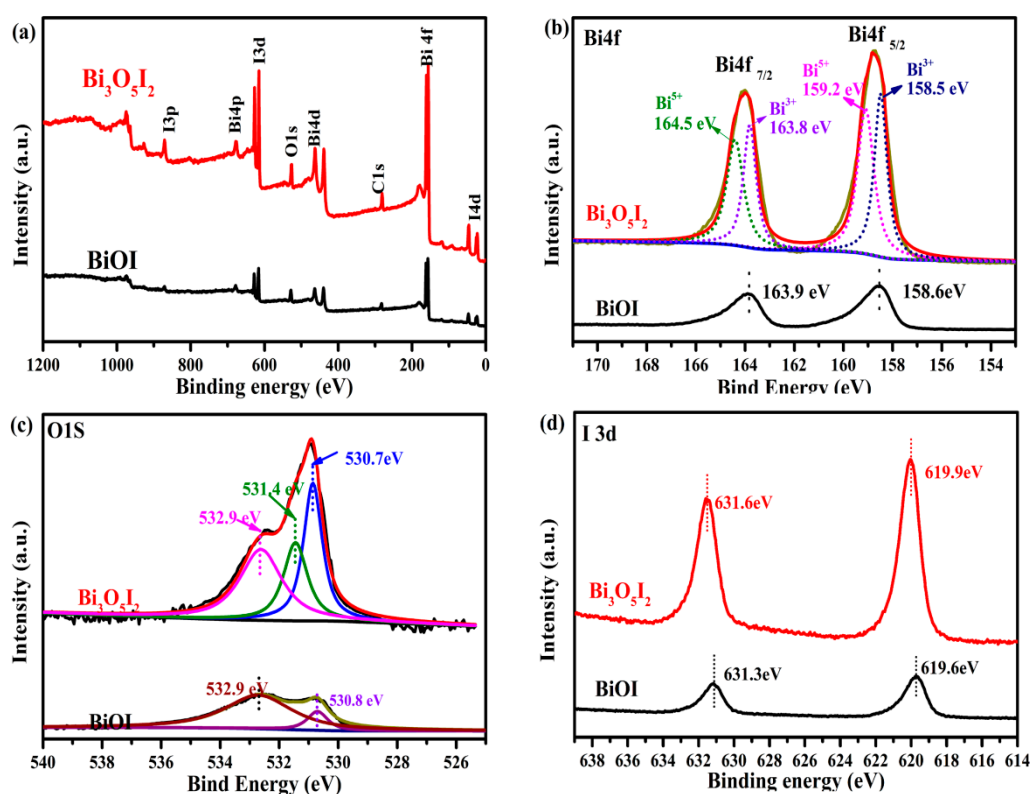


Figure 5. XPS spectra of $\text{Bi}_3\text{O}_5\text{I}_2$ and BiOI: (a) Survey, (b) Bi 4f, (c) O 1s, (d) I 3d.

As shown in Figure 6, the specific surface area and the pore size distribution of $\text{Bi}_3\text{O}_5\text{I}_2$ and BiOI were analyzed by the N_2 absorption and desorption analysis. It was clear to see that all the isotherms were type IV, which exhibited the presence of mesoporous [43]. The hysteresis loop located at the range of 0.5–1.0 P/P_0 were ascribed to type H_3 in the IUPAC classification, indicating that the mesoporous could be considered as accumulated pores of the sample nanosheets [43]. Moreover, the hysteresis loop shifts approach $P/P_0 = 1$, implying the existence of macroporous (>50 nm). The BET specific surface area of the $\text{Bi}_3\text{O}_5\text{I}_2$ was $26.81 \text{ m}^2/\text{g}$, while the surface area of BiOI was $13 \text{ m}^2/\text{g}$, possibly due to its hollow microsphere structure. The PSD curves showed that the pore size range of $\text{Bi}_3\text{O}_5\text{I}_2$ and BiOI was 2–140 nm. The main pore size of $\text{Bi}_3\text{O}_5\text{I}_2$ was 21 nm, while the main pore size of BiOI was 39 nm. To our best knowledge, the larger specific surface area can lead to the increase of photocatalytic reaction sites [37]. Therefore, it could be concluded that the $\text{Bi}_3\text{O}_5\text{I}_2$ might have a higher photocatalytic activity than BiOI.

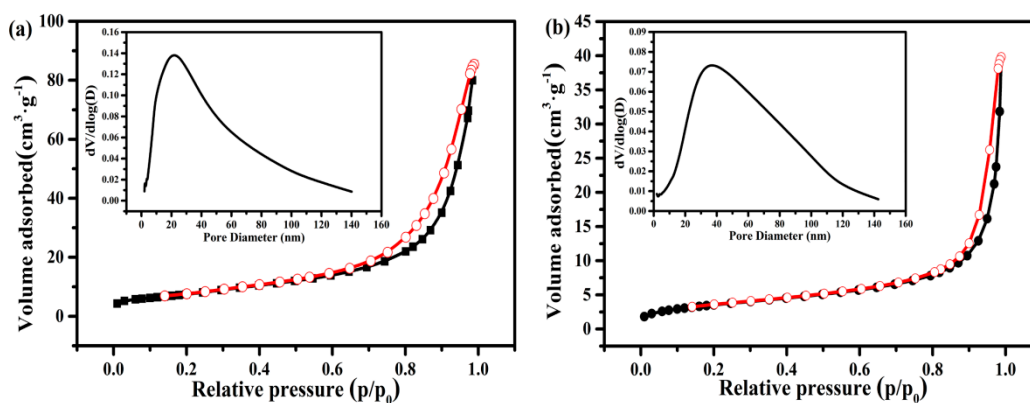


Figure 6. Nitrogen absorption-desorption isotherms and the pore-size distribution (inset) of (a) $\text{Bi}_3\text{O}_5\text{I}_2$ and (b) BiOI.

2.3. Optical Property and Photoelectric Property of the Photocatalysts

The UV-vis diffuse reflectance spectroscopy of $\text{Bi}_3\text{O}_5\text{I}_2$ and BiOI was shown in Figure 7a. In comparison with BiOI , $\text{Bi}_3\text{O}_5\text{I}_2$ had a clearly blue shift in the absorption edge, indicating $\text{Bi}_3\text{O}_5\text{I}_2$ had a higher energy gap (E_g). This agrees with the results of the I-deficient bismuth oxyiodide reported in the previous literature [46,47]. Meanwhile, the DRS displayed that the absorption band edge of $\text{Bi}_3\text{O}_5\text{I}_2$ was 586 nm, which indicated that $\text{Bi}_3\text{O}_5\text{I}_2$ had a good visible light absorption [29].

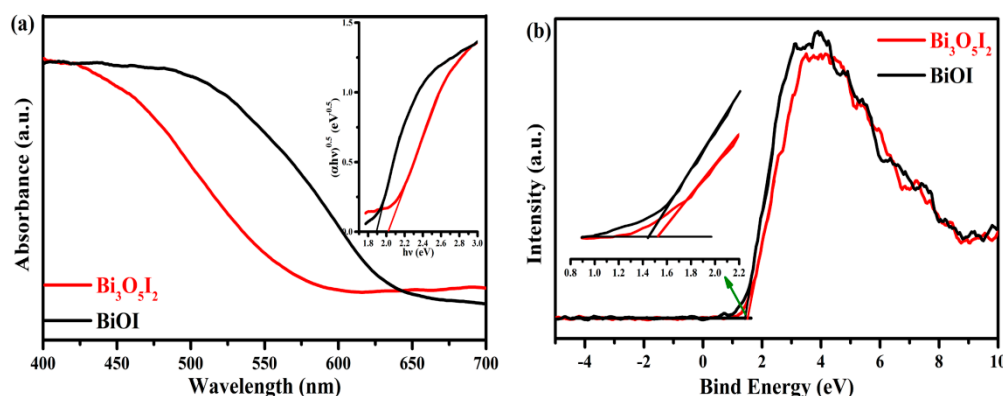


Figure 7. (a) Diffuse reflectance spectra and band gaps of $\text{Bi}_3\text{O}_5\text{I}_2$ and BiOI (inset), (b) valence band XPS spectra of $\text{Bi}_3\text{O}_5\text{I}_2$ and BiOI .

To estimate the E_g value of $\text{Bi}_3\text{O}_5\text{I}_2$, a classical Tauc approach was introduced. According to the equation $\alpha h\nu = K(h\nu - E_g)^{n/2}$ (α , $h\nu$, K and E_g are the absorption coefficient, the energy of irradiation light, a constant and band gap energy, respectively), the E_g value can be calculated [43]. Considering BiOI and $\text{Bi}_3\text{O}_5\text{I}_2$, were indirect transition semiconductor, the value of n is 4 [31,32,34]. The band gaps of $\text{Bi}_3\text{O}_5\text{I}_2$ was calculated to be 2.02 eV and higher than that of BiOI (1.89 eV). In order to determine the relative positions of the valence band edge (VB), the VB-XPS spectra of $\text{Bi}_3\text{O}_5\text{I}_2$ and BiOI were measured and shown in Figure 7b. The VB edge of $\text{Bi}_3\text{O}_5\text{I}_2$ and BiOI was 1.50 eV and 1.42 eV. The conduction band (CB) edge of $\text{Bi}_3\text{O}_5\text{I}_2$ and BiOI could be obtained using the equation of $E_{CB} = E_{VB} - E_g$. Therefore, the CB positions of $\text{Bi}_3\text{O}_5\text{I}_2$ and BiOI were -0.72 eV and -0.47 eV. The suitable band energy of $\text{Bi}_3\text{O}_5\text{I}_2$ compared to BiOI implied that $\text{Bi}_3\text{O}_5\text{I}_2$ has a stronger oxidation and reduction ability than BiOI [43]. As we all know, the electron in the less positive conduction band edge (CB) has higher reduction ability and the hole in the more positive valence band edge (VB) has higher oxidation ability. As we all know, the electron in the less positive conduction band edge (CB) has higher reduction ability and the hole in the more positive valence band edge (VB) has higher oxidation ability. Therefore, $\text{Bi}_3\text{O}_5\text{I}_2$ with the less positive CB position and more positive VB position had the promising photocatalytic activity than BiOI . The energy band structure of $\text{Bi}_3\text{O}_5\text{I}_2$ and BiOI were shown in Figure S2. The conduction band edge (CB) and the valence band edge (VB) of $\text{Bi}_3\text{O}_5\text{I}_2$ were -0.72 eV and 1.50 eV (versus normal hydrogen electrode (NHE)). Since the CB value of $\text{Bi}_3\text{O}_5\text{I}_2$ was less positive than $E^0(\text{O}_2/\bullet\text{O}_2^-)$ (-0.046 eV vs. NHE) and the VB value of $\text{Bi}_3\text{O}_5\text{I}_2$ was more positive than $E^0(\bullet\text{OH}/\text{OH}^-)$ (2.38 eV vs. NHE) [48], the photogenerated electrons can reduce O_2 to $\bullet\text{O}_2^-$ and the photogenerated holes cannot oxidize OH^- to $\bullet\text{OH}$. Meanwhile, the VB value of $\text{Bi}_3\text{O}_5\text{I}_2$ was more positive than the redox potential of MO (1.48 eV versus NHE) [49], the photogenerated holes can oxidize MO directly. The result of active species experiments shown in Figure 11 further confirm the above results. Based on the band structure analysis, $\text{Bi}_3\text{O}_5\text{I}_2$ would exhibit effective photocatalytic performance, owing to its strong oxidation and reduction ability.

The transient photocurrent responses and electrochemical impedance spectroscopy (EIS) were further explored to estimate the generation and recombination rate of photogenerated electron-hole pairs, which was displayed in Figure 8. In Figure 8a, it was worth noting that the photocurrent density of the $\text{Bi}_3\text{O}_5\text{I}_2$ electrode is much higher than BiOI for each switch-on and -off event. The enhanced

photocurrent response of the $\text{Bi}_3\text{O}_5\text{I}_2$ indicated a lower recombination of photogenerated electron-hole pairs than pure BiOI [50]. The photocurrent response mainly depends on the generation rate of photoinduced electron-hole pairs and the recombination rate of photogenerated electron-hole pairs. Meanwhile, the recombination rate of photogenerated electron-hole pairs were the rate controlling step of the photocurrent response. Just shown in Figure 7a, BiOI had a superior light harvesting than the I-deficient bismuth oxyiodides. It indicates that BiOI might have a higher generation rate of photoinduced electron-hole pairs than $\text{Bi}_3\text{O}_5\text{I}_2$. However, it should be noted that the recombination rate of photogenerated electron-hole pairs of BiOI was much higher than $\text{Bi}_3\text{O}_5\text{I}_2$. Therefore, the photocurrent response of $\text{Bi}_3\text{O}_5\text{I}_2$ is stronger than that of BiOI. The result of the electrochemical impedance spectroscopy (EIS) of BiOI and $\text{Bi}_3\text{O}_5\text{I}_2$ shown in Figure 8b can verify this result. $\text{Bi}_3\text{O}_5\text{I}_2$ had a smaller arc radius of the EIS Nyquist plot than BiOI, suggesting an effective separation of photoinduced electron-hole pairs and fast interfacial charge transfer than BiOI [11]. In conclusion, $\text{Bi}_3\text{O}_5\text{I}_2$ has a more efficient photocatalytic performance than BiOI.

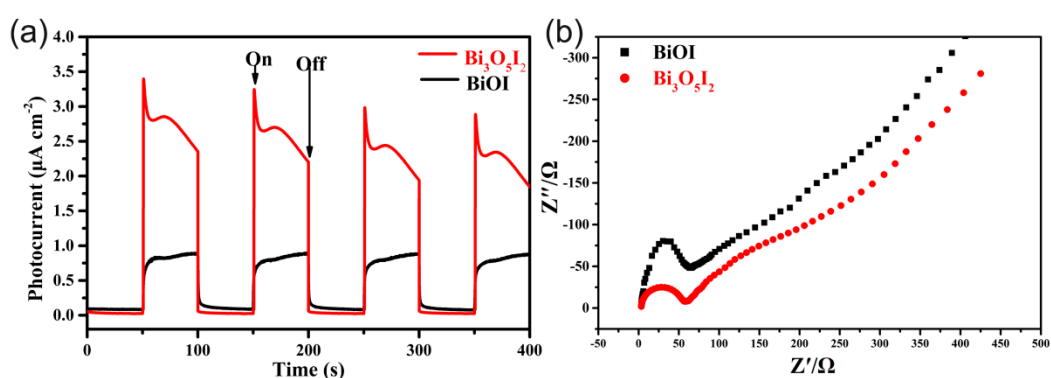


Figure 8. (a) Photocurrent responses of $\text{Bi}_3\text{O}_5\text{I}_2$ and BiOI in Na_2SO_4 solutions, (b) electrochemical impedance spectroscopy of $\text{Bi}_3\text{O}_5\text{I}_2$ and BiOI.

2.4. Photocatalytic Performance of the Photocatalysts

The photocatalytic ability of $\text{Bi}_3\text{O}_5\text{I}_2$ were measured on the decomposing of MO (20 mg/L) in water under the simulated visible light, which was shown in Figure 9. In Figure 9a, the maximum absorption of MO shifted from 464 nm to 420 nm in the presence of $\text{Bi}_3\text{O}_5\text{I}_2$ after irradiation for 180 min [37]. Meanwhile, the color of MO changed from yellow to colorless during the photocatalytic reaction, which indicated that MO was degraded by $\text{Bi}_3\text{O}_5\text{I}_2$ under the simulated solar light irradiation.

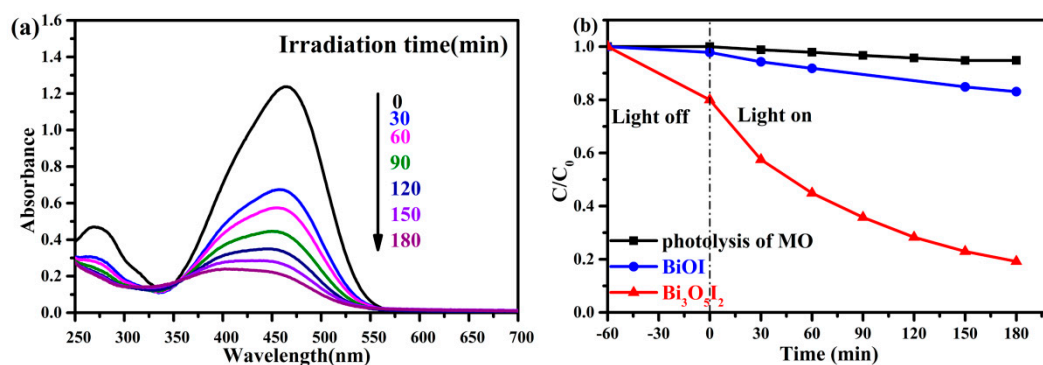


Figure 9. (a) The UV-Vis absorption spectral changes during the degradation of MO (20 mg/L), (b) photocatalytic decomposition of MO in the presence of $\text{Bi}_3\text{O}_5\text{I}_2$ and BiOI and photolysis of MO under simulated visible light irradiation.

The variation of the MO content with the irradiation time was shown in Figure 9b. It can be seen that 81% of MO was photodegraded by Bi₃O₅I₂ while only 11% of MO was degraded by BiOI. This confirmed that Bi₃O₅I₂ present higher photoactivities than BiOI. Moreover, it was much higher than most of the activity data over other similar catalysts reported in previous works, as compared in Table S3.

The quantum efficiency of the photocatalytic activity is important for the photocatalysts. However, there is little information about the quantity of electrons needed to degrade a methyl orange molecule in literatures. Additionally it is also difficult to measure it in our Lab. In order to calculate the quantum efficiency (QE) of Bi₃O₅I₂ and BiOI, the following equation about the apparent QE is put forward according to the literature and the calculated process is listed below in detail [12].

The photocatalytic reaction conditions: 100 mL, 20 mg/L methyl orange (MO 327.334 g/mol) solvent, the moles of MO is 6.11×10^{-6} mol. A light ($\lambda \sim 420$ nm) was used and the light intensity was $300 \text{ mW}\cdot\text{cm}^{-2}$. The energy can be obtained on the surface (1.3 cm^{-2}) of the reaction mixture solution. We assumed that it takes m electrons to degrade a methyl orange molecule. n % of MO was degraded after the t hour. The apparent QE detected under the same photocatalytic reaction condition and calculated to the equation as below:

$$\begin{aligned} \text{QE} &= \frac{\text{number of reacted electrons}}{\text{number of incident photons}} \times 100\% = \frac{6.11 \times 10^{-6} \text{ mol} \times m \times n\%}{\frac{E}{h\nu}} = \frac{6.11 \times 10^{-6} \text{ mol} \times m \times n\% \times hc}{E\lambda} \\ &= \frac{6.11 \times 10^{-6} \times m \times n\% \times 6.02 \times 10^{23} \times 6.63 \times 10^{-34} \times 3 \times 10^8}{300 \times 1.3 \times 10^{-3} \times t \times 3600 \times 420 \times 10^{-9}} \\ &= 0.00124 \frac{m \times n\%}{t} \end{aligned}$$

When $m = 1$, it can be found that the QE of Bi₃O₅I₂ and BiOI were 0.033% and 0.005% at 420 nm.

Based on the above analysis, the high photocatalytic activity of Bi₃O₅I₂ should be ascribed to its hollow structure, suitable band structure and efficient separation of photogenerated electron–hole pairs. Firstly, with a hole in microspheres, Bi₃O₅I₂ has a larger surface area ($26.81 \text{ m}^2/\text{g}$) than BiOI ($13.00 \text{ m}^2/\text{g}$). With a higher surface area, Bi₃O₅I₂ had more active sites and absorb more MO on its surface. Moreover, the high surface area of hollow structures could promote the transfer of photoinduced carriers to the surface and enhance the decomposition of MO [37]. Secondly, Bi₃O₅I₂ had a higher CB position and lower VB location than BiOI, which enable the photogenerated electron and hole of the Bi₃O₅I₂ strong oxidation capability [9]. Thirdly, the photocurrent spectra showed that Bi₃O₅I₂ had a lower recombination of photoinduced carriers under the simulated light irradiation. Therefore, Bi₃O₅I₂ should have an enhanced photocatalytic performance since the photocatalytic activity of the photocatalyst mainly depend on the charge carrier generation and separation [9].

2.5. The Lifetime eValuation of the Photocatalysts

The reusability of the Bi₃O₅I₂ material was investigated by recycling and reusing the catalyst (in Figure 10). Figure 10a shows no distinct loss in the photocatalytic activity when MO was degraded for the fourth time. Therefore, the Bi₃O₅I₂ exhibited an excellent stability during the degradation of MO.

In order to evaluate the structural stability of Bi₃O₅I₂, the fresh and used Bi₃O₅I₂ were characterized by the XRD. The result was shown in Figure 10b. Obviously, there was no apparent change for the recycled Bi₃O₅I₂ compared with the fresh Bi₃O₅I₂, indicating the Bi₃O₅I₂ are stable and reusable. Owing to its good photocatalytic activity as well as its stable and reusable character, Bi₃O₅I₂ shows great potential for the photocatalytic degradation of organic pollutants in waste water.

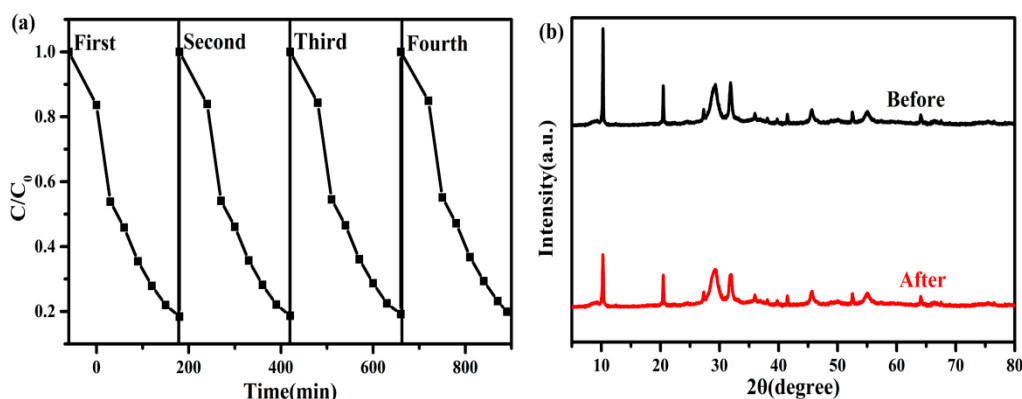


Figure 10. (a) Recycling measurements for Bi₃O₅I₂, (b) XRD patterns of the Bi₃O₅I₂ before and after the cycling photocatalytic experiments.

2.6. The Possible Photocatalytic Mechanism

The probe mechanism Bi₃O₅I₂ was further evaluated by the radicals and holes trapping experiments and the result was shown in Figure 11. Benzoquinone (BQ) was used as the quenching agent of superoxide radical ($\bullet\text{O}_2^-$). Potassium iodide (KI) was used as the scavenger of hole (h^+) and hydroxyl radical ($\bullet\text{OH}$). Tert-butyl alcohol (TBA) was used as the quenching agent of $\bullet\text{OH}$. Their concentrations in the MO solution were 0.1 mM/L. Figure 11 showed that the degradation of MO was obviously decreased from 81% to 55% in the presence of KI, indicating that h^+ or $\bullet\text{OH}$ played an important role for degrading MO [51]. While, the addition of TBA did not influence the MO degradation efficiency, indicating that $\bullet\text{OH}$ has no effect on the degrading MO. Therefore, it could be inferred that h^+ was the major active species for the degradation of MO. When BQ was added, the MO degradation efficiency decreased significantly from 81% to 29%, suggesting that $\bullet\text{O}_2^-$ played the key role for degrading MO. In conclusion, $\bullet\text{O}_2^-$ was the primary active species and h^+ was the main active species in the degradation of MO.

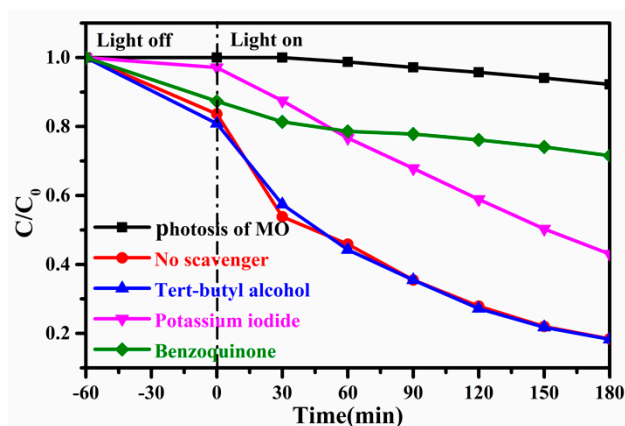
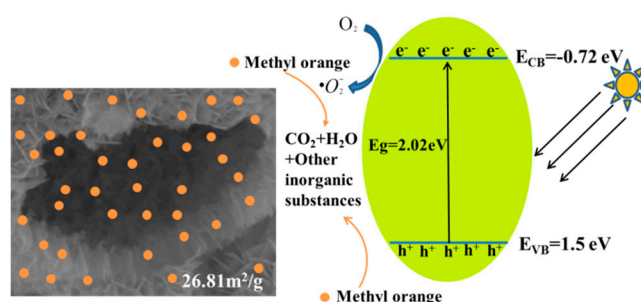


Figure 11. Photocatalytic degradation of MO by the Bi₃O₅I₂ under the presence of different scavenging species.

In conclusion of the analysis above, a possible photocatalytic program was proposed, which was displayed in Scheme 1. Firstly, the MO molecules were absorbed on the surface of the Bi₃O₅I₂. Secondly, when the Bi₃O₅I₂ was irradiated by simulated visible light, the photogenerated electron would transfer from the valence band to the conduction band, leaving h^+ in the valence band and electrons in the conduction band. Thirdly, h^+ are capable of oxidizing MO directly and the electrons were also believed to be capable of benefiting the oxidation process through reduction of the absorbed O₂ into

$\bullet\text{O}_2^-$. As a result, the MO molecular was demineralized to CO_2 , H_2O and other inorganic substances by the $\bullet\text{O}_2^-$ and h^+ .



Scheme 1. Hollow structure of $\text{Bi}_3\text{O}_5\text{I}_2$ composite and probe processes of the photodegradation of MO over the $\text{Bi}_3\text{O}_5\text{I}_2$ composite.

3. Materials and Method

3.1. Materials

The bismuth nitrate pentahydrate (99.5 %, Sinopharm Chemical Reagent Co., Ltd. Shanghai, China), potassium iodide (99.5 %, Sinopharm Chemical Reagent Co., Ltd. Shanghai, China), ethyl alcohol and ethylene glycol (99.0 %, Sinopharm Chemical Reagent Co., Ltd. Shanghai, China) were used as received. The distilled water was synthesized by the water purification system.

3.2. Synthesis of the $\text{Bi}_3\text{O}_5\text{I}_2$ and BiOI

In a typical synthesis route, 0.004 mol of bismuth nitrate pentahydrate and 0.004 mol of potassium iodide (KI) was dissolved in 40 mL of ethylene glycol under vigorously stirring for 0.5 h, respectively. After that, the KI solution was added dropwise into the solution which contained bismuth nitrate. Then, the mixture solution was stirred vigorously for 0.5 h at 25 °C and transferred into a 100 mL Teflon-lined stainless autoclave. The Teflon-lined stainless autoclave was heated to 160 °C and maintained for 12 h in a homogeneous reactor and air-cooled to room temperature. The synthesized precipitates were centrifuged and washed three times by ethanol and deionized water, and dried at 80 °C for 12 h in air. The sample was labelled as the I-deficient bismuth oxyiodide. Meanwhile, BiOI was prepared with the method above except using distilled water as the solvent of KI.

3.3. Photocatalyst Characterization

The samples are tested by the X-ray diffraction (XRD) with a D8 ADVANCE X-ray diffractometer (Cu $K\alpha$ radiation, $\lambda = 1.54178 \text{ \AA}$ Karlsruhe, German). A field emission scanning electron microscope (FE-SEM, JSM-7001F, Kyoto, Japan) was used to characterize the morphology of the samples. The FE-SEM was equipped with an energy dispersive analysis system of the X-ray spectroscopy (EDS) as well as an elemental mapping system. The images of the transmission electron microscopy (TEM) for the samples were from a JEOL (JEM-2100F, Kyoto, Japan) operating at 200 kV. The N_2 adsorption and desorption isotherms were investigated by a Tristar II 3020 sorptometer (Atlanta, GA, USA). The operating condition is at 77 K with the samples degassed at 100 °C in vacuo. The XPS spectrum was obtained with a KRATOS X-ray photoelectron spectroscopy (AXIS ULTRA DLD, Manchester, UK). The diffuse reflectance UV–vis absorbance spectroscopy were recorded by using a spectrophotometer (Shimadzu UV-2550, Kyoto, Japan) BaSO_4 as the reference. The thermogravimetric analysis (TG) was carried out with a Netzsch STA 449C (Free State of Bavaria, German). In addition, the samples were heated with 10 °C/min from 25 °C to 900 °C in air atmosphere. The content of Bi was estimated by an Inductive Coupled Plasma emission spectrometer (Thermo iCAP6300, Waltham, MA, USA). The CHI

660E electrochemical system (Shanghai, China) was used for photoelectrochemical and electrochemical measurements and the sample preparation process was the same with the previous report [52].

3.4. Test of Photocatalytic Activity

To evaluate the photocatalytic activities of the as prepared samples, the photocatalytic degradation of MO was used under simulated visible light with a radiation source of the 300 W Xe lamp (PLS-SXE 300, Beijing, China). A 250 mL home-made reactor combined with a cooling water system was used. In each experiment, 100 mL of the MO solution (20 mg/L) was put in the reactor. A 25 mg catalyst was added into the MO solution. After that, the mixture of the MO solution and 25 mg catalyst placed in the dark was stirred for 60 min. Then, the mixture was exposed to simulated solar light with stirring. During the process, a 5 mL mixture was sampled at 30 min intervals. In addition, the concentration of MO in the mixture was measured by a UV–visible spectrophotometer. The spectrophotometer is the UV-2550 of Shimadzu, Japan, operating at 464 nm with water as a reference.

4. Conclusions

In summary, a new I-deficient bismuth oxyiodide $\text{Bi}_3\text{O}_5\text{I}_2$ with a hollow structure was successfully prepared by an ethylene glycol-assisted solvothermal process. The average diameter of the $\text{Bi}_3\text{O}_5\text{I}_2$ hollow microspheres was 1–3 μm , and the hollow nature contribute to the larger BET specific surface area than BiOI. The $\text{Bi}_3\text{O}_5\text{I}_2$ presented a higher photocatalytic performance on the degradation of MO under simulated solar light irradiation than BiOI did. The enhanced photocatalytic activities of $\text{Bi}_3\text{O}_5\text{I}_2$ could be contributed to its hollow structure, its appropriate band-gap and its low recombination rate of photogenerated carriers. The $\bullet\text{O}_2^-$ and h^+ was the main active specie in the degradation of MO. The result of the stable and reusable performance indicated that $\text{Bi}_3\text{O}_5\text{I}_2$ showed great potential for the photocatalytic degradation of organic pollutants in waste water.

Supplementary Materials: The following are available online at <http://www.mdpi.com/2073-4344/9/9/709/s1>. Figure S1: SEM images and EDS analysis of as prepared samples in different locations: (a), (b) I-poor bismuth oxyiodide, (c), (d) BiOI, Figure S2: The energy band structure of $\text{Bi}_3\text{O}_5\text{I}_2$ and BiOI, Table S1: The elemental composition of I-poor bismuth oxyiodide, Table S2: The elemental composition of BiOI, Table S3 Photocatalytic activity of different researches.

Author Contributions: B.C. designed and performed the experiments; B.C., Z.L., H.C. and J.W. analyzed the data; L.Z. provided financial support; B.C. wrote the paper; H.D. and X.L. reviewed and edited the paper.

Funding: This research was funded by the Science and Technology Major Project of Shanxi Province (No. 20181101018).

Conflicts of Interest: The authors declare no conflict of interest.

References

1. Peng, Y.; Yu, P.-P.; Zhou, H.-Y.; Xu, A.-W. Synthesis of BiOI/Bi₄O₅I₂/Bi₂O₂CO₃ p–n–p heterojunctions with superior photocatalytic activities. *New J. Chem.* **2015**, *39*, 8321–8328. [[CrossRef](#)]
2. Dong, F.; Xiong, T.; Sun, Y.; Zhang, Y.X.; Zhou, Y. Controlling interfacial contact and exposed facets for enhancing photocatalysis via 2D–2D heterostructures. *Chem. Commun.* **2015**, *51*, 8249–8252. [[CrossRef](#)] [[PubMed](#)]
3. Wang, L.; Liu, X. Fast Degradation of Monochloroacetic Acid by BiOI-Enhanced UV/S(IV) Process: Efficiency and Mechanism. *Catalysts* **2019**, *9*, 460. [[CrossRef](#)]
4. Liu, H.; Cao, W.-R.; Su, Y.; Chen, Z.; Wang, Y. Bismuth oxyiodide–graphene nanocomposites with high visible light photocatalytic activity. *J. Colloid Interface Sci.* **2013**, *398*, 161–167. [[CrossRef](#)] [[PubMed](#)]
5. Cheng, H.; Huang, B.; Dai, Y. Engineering BiOX (X = Cl, Br, I) nanostructures for highly efficient photocatalytic applications. *Nanoscale* **2014**, *6*, 2009. [[CrossRef](#)] [[PubMed](#)]
6. Zhu, G.; Hojamberdiev, M.; Zhang, S.; Din, S.T.U.; Yang, W. Enhancing visible-light-induced photocatalytic activity of BiOI microspheres for NO removal by synchronous coupling with Bi metal and graphene. *Appl. Surf. Sci.* **2019**, *467*, 968–978. [[CrossRef](#)]

7. Ye, L.; Jin, X.; Ji, X.; Liu, C.; Su, Y.; Xie, H.; Liu, C. Facet-dependent photocatalytic reduction of CO₂ on BiOI nanosheets. *Chem. Eng. J.* **2016**, *291*, 39–46. [[CrossRef](#)]
8. Long, Y.; Wang, Y.; Zhang, D.; Ju, P.; Sun, Y. Facile synthesis of BiOI in hierarchical nanostructure preparation and its photocatalytic application to organic dye removal and biocidal effect of bacteria. *J. Colloid Interface Sci.* **2016**, *481*, 47–56. [[CrossRef](#)]
9. Lee, G.-J.; Zheng, Y.-C.; Wu, J.J. Fabrication of hierarchical bismuth oxyhalides (BiOX, X = Cl, Br, I) materials and application of photocatalytic hydrogen production from water splitting. *Catal. Today* **2018**, *307*, 197–204. [[CrossRef](#)]
10. Dai, W.W.; Zhao, Z.Y. Electronic structure and optical properties of BiOI as a photocatalyst driven by visible light. *Catalysts* **2016**, *6*, 133. [[CrossRef](#)]
11. Huang, H.; Xiao, K.; Zhang, T.; Dong, F.; Zhang, Y. Rational design on 3D hierarchical bismuth oxyiodides via in situ self-template phase transformation and phase-junction construction for optimizing photocatalysis against diverse contaminants. *App. Catal. B Environ.* **2017**, *203*, 879–888. [[CrossRef](#)]
12. Bai, Y.; Chen, T.; Wang, P.; Wang, L.; Ye, L. Bismuth-rich Bi₄O₅X₂ (X = Br, and I) nanosheets with dominant {101} facets exposure for photocatalytic H₂ evolution. *Chem. Eng. J.* **2016**, *304*, 454–460. [[CrossRef](#)]
13. Hu, J.; Weng, S.; Zheng, Z.; Pei, Z.; Huang, M.; Liu, P. Solvents mediated-synthesis of BiOI photocatalysts with tunable morphologies and their visible-light driven photocatalytic performances in removing of arsenic from water. *J. Hazard. Mater.* **2014**, *264*, 293–302. [[CrossRef](#)]
14. Cao, J.; Zhou, C.; Lin, H.; Xu, B.; Chen, S. Direct hydrolysis preparation of plate-like BiOI and their visible light photocatalytic activity for contaminant removal. *Mater. Lett.* **2013**, *109*, 74–77. [[CrossRef](#)]
15. Di, J.; Xia, J.; Ge, Y.; Xu, L.; Xu, H.; He, M.; Zhang, Q.; Li, H. Reactable ionic liquid-assisted rapid synthesis of BiOI hollow microspheres at room temperature with enhanced photocatalytic activity. *J. Mater. Chem. A* **2014**, *2*, 15864–15874. [[CrossRef](#)]
16. Zhang, G.; Su, A.; Qu, J.; Xu, Y. Synthesis of BiOI flowerlike hierarchical structures toward photocatalytic reduction of CO₂ to CH₄. *Mater. Res. Bull.* **2014**, *55*, 43–47. [[CrossRef](#)]
17. Han, J.; Zhu, G.; Hojamberdiev, M.; Peng, J.; Zhang, X.; Liu, Y.; Ge, B. Rapid adsorption and photocatalytic activity for Rhodamine B and Cr(vi) by ultrathin BiOI nanosheets with highly exposed {001} facets. *New J. Chem.* **2015**, *39*, 1874–1882. [[CrossRef](#)]
18. Shan, L.-W.; He, L.-Q.; Suriyaprakash, J.; Yang, L.-X. Photoelectrochemical (PEC) water splitting of BiOI{001} nanosheets synthesized by a simple chemical transformation. *J. Alloys Compd.* **2016**, *665*, 158–164. [[CrossRef](#)]
19. Huang, H.; Xiao, K.; He, Y.; Zhang, T.; Dong, F.; Du, X.; Zhang, Y. In situ assembly of BiOI@Bi₁₂O₁₇Cl₂ p–n junction: Charge induced unique front-lateral surfaces coupling heterostructure with high exposure of BiOI {001} active facets for robust and nonselective photocatalysis. *Appl. Catal. B Environ.* **2016**, *199*, 75–86. [[CrossRef](#)]
20. Zeng, L.; Zhe, F.; Wang, Y.; Zhang, Q.; Zhao, X.; Hu, X.; Wu, Y.; He, Y. Preparation of interstitial carbon doped BiOI for enhanced performance in photocatalytic nitrogen fixation and methyl orange degradation. *J. Colloid Interf. Sci.* **2019**, *539*, 563–574. [[CrossRef](#)]
21. Dai, B.; Zhang, A.; Liu, Z.; Wang, T.; Li, C.; Zhang, C.; Li, H.; Liu, Z.; Zhang, X. Facile synthesis of metallic Bi deposited BiOI composites with the aid of EDTA-2Na for highly efficient Hg⁰ removal. *Catal. Commun.* **2019**, *121*, 53–56. [[CrossRef](#)]
22. Liu, H.; Cao, W.; Su, Y.; Wang, Y.; Wang, X. Synthesis, characterization and photocatalytic performance of novel visible-light-induced Ag/BiOI. *Appl. Catal. B Environ.* **2012**, *111*, 271–279. [[CrossRef](#)]
23. Huang, H.; Liu, K.; Zhang, Y.; Chen, K.; Zhang, Y.; Tian, N. Tunable 3D hierarchical graphene–BiOI nanoarchitectures: Their in situ preparation, and highly improved photocatalytic performance and photoelectrochemical properties under visible light irradiation. *RSC Adv.* **2014**, *4*, 49386–49394. [[CrossRef](#)]
24. Shi, X.; Wang, P.; Wang, L.; Bai, Y.; Xie, H.; Zhou, Y.; Ye, L. Change in photocatalytic NO removal mechanisms of ultrathin BiOBr/BiOI via NO₃-adsorption. *Appl. Catal. B Environ.* **2019**, *243*, 322–329. [[CrossRef](#)]
25. Al-Keisy, A.; Ren, L.; Xu, X.; Hao, W.; Dou, S.X.; Du, Y. Selective ferroelectric BiOI/Bi₄Ti₃O₁₂ heterostructures for visible light-driven photocatalysis. *J. Phys. Chem. C* **2019**, *123*, 517–525. [[CrossRef](#)]
26. Yan, P.; Jiang, D.; Li, H.; Cheng, M.; Xu, L.; Qian, J.; Bao, J.; Xia, J.; Li, H. Exploitation of a photoelectrochemical sensing platform for catechol quantitative determination using BiPO₄ nanocrystals/BiOI heterojunction. *Anal. Chim. Acta* **2018**, *1042*, 11–19. [[CrossRef](#)]

27. Gao, P.; Yan, T.; Liu, H.; Sun, M.; Wei, Q.; Xu, W.; Wang, X.; Du, B. Facile synthesized highly active BiOI/Zn₂GeO₄ composites for the elimination of endocrine disrupter BPA under visible light irradiation. *New J. Chem.* **2015**, *39*, 3964–3972.
28. Jin, X.; Lv, C.; Zhou, X.; Zhang, C.; Meng, Q.; Liu, Y.; Chen, G. Molecular adsorption promotes carrier migration: Key step for molecular oxygen activation of defective Bi₄O₅I₂. *Appl. Catal. B Environ.* **2018**, *226*, 53–60. [[CrossRef](#)]
29. Cao, J.; Li, X.; Lin, H.; Xu, B.; Luo, B.; Chen, S. Low temperature synthesis of novel rodlike Bi₅O₇I with visible light photocatalytic performance. *Mater. Lett.* **2012**, *76*, 181–183. [[CrossRef](#)]
30. Dai, B.J.; Zhang, A.C.; Zhang, D.; Liu, Z.C.; Li, H.X.; Wang, R.R.; Zhang, X.M. Effect of preparation method on the structure and photocatalytic performance of BiOI and Bi₅O₇I for Hg-0 removal. *Atmos. Pollut. Res.* **2019**, *10*, 355–362. [[CrossRef](#)]
31. Sun, S.M.; Wang, W.Z.; Zhang, L.; Zhou, L.; Yin, W.Z.; Shang, M. Visible light-induced efficient contaminant removal by Bi₅O₇I. *Environ. Sci. Technol.* **2009**, *43*, 2005–2010. [[CrossRef](#)]
32. Chuang, C.-W.; Siao, C.-W.; Lee, W.W.; Lu, C.-S.; Chen, Y.-J.; Fu, J.-Y. Synthesis of bismuth oxyiodides and their composites: Characterization, photocatalytic activity, and degradation mechanisms. *RSC Adv.* **2015**, *5*, 23450–23463.
33. Xiao, X.; Zhang, W.D. Hierarchical Bi₇O₉I₃ micro/nano-architecture: Facile synthesis, growth mechanism, and high visible light photocatalytic performance. *Rsc. Adv.* **2011**, *1*, 1099–1105. [[CrossRef](#)]
34. Xiao, X.; Xing, C.; He, G.; Zuo, X.; Nan, J.; Wang, L. Solvothermal synthesis of novel hierarchical Bi₄O₅I₂ nanoflakes with highly visible light photocatalytic performance for the degradation of 4-tert-butylphe. *Appl. Catal. B Environ.* **2014**, *148*, 154–163. [[CrossRef](#)]
35. Zhang, L.; Gonçalves, A.A.S.; Jiang, B.; Jaroniec, M. Capture of Iodide by Bismuth Vanadate and Bismuth Oxide: An Insight into the Process and its Aftermath. *ChemSusChem* **2018**, *11*, 1486–1493. [[CrossRef](#)]
36. Liu, Q.-C.; Ma, D.-K.; Hu, Y.-Y.; Zeng, Y.-W.; Huang, S.-M. Various Bismuth Oxyiodide Hierarchical Architectures: Alcohothermal-Controlled Synthesis, Photocatalytic Activities, and Adsorption Capabilities for Phosphate in Water. *ACS Appl. Mater. Interfaces* **2013**, *5*, 11927–11934. [[CrossRef](#)]
37. Xia, J.; Yin, S.; Li, H.; Xu, H.; Yan, Y.; Zhang, Q. Self-Assembly and Enhanced Photocatalytic Properties of BiOI Hollow Microspheres via a Reactable Ionic Liquid. *Langmuir* **2011**, *27*, 1200–1206. [[CrossRef](#)]
38. Ma, D.-K.; Zhou, S.-M.; Hu, X.; Jiang, Q.-R.; Huang, S.-M. Hierarchical BiOI and hollow Bi₂WO₆ microspheres: Topochemical conversion and photocatalytic activities. *Mater. Chem. Phys.* **2013**, *140*, 11–15. [[CrossRef](#)]
39. Zhang, K.; Zhang, D.; Liu, J.; Ren, K.; Luo, H.; Peng, Y.; Li, G.; Yu, X. A novel nanoreactor framework of iodine-incorporated BiOCl core-shell structure: Enhanced light-harvesting system for photocatalysis. *CrystEngComm* **2012**, *14*, 700–707. [[CrossRef](#)]
40. Ji, M.; Xia, J.; Di, J.; Wang, B.; Yin, S.; Xu, L.; Zhao, J.; Li, H. Ionic liquid-assisted bidirectional regulation strategy for carbon quantum dots (CQDs)/Bi₄O₅I₂ nanomaterials and enhanced photocatalytic properties. *J. Colloid Interface Sci.* **2016**, *478*, 324–333. [[CrossRef](#)]
41. Tu, S.; Zheng, C.; Zhong, H.; Lu, M.; Xiao, X.; Zuo, X.; Nan, J. Flower-like Bi₄O₅I₂/Bi₅O₇ I nanocomposite: Facile hydrothermal synthesis and efficient photocatalytic degradation of propylparaben under visible-light irradiation. *RSC Adv.* **2016**, *6*, 44552–44560. [[CrossRef](#)]
42. Ren, K.; Zhang, K.; Liu, J.; Luo, H.; Huang, Y.; Yu, X. Controllable synthesis of hollow/flower-like BiOI microspheres and highly efficient adsorption and photocatalytic activity. *CrystEngComm* **2012**, *14*, 4384. [[CrossRef](#)]
43. Liu, C.; Wang, X.-J. Room temperature synthesis of Bi₄O₅I₂ and Bi₅O₇I ultrathin nanosheets with a high visible light photocatalytic performance. *Dalton Trans.* **2016**, *45*, 7720–7727. [[CrossRef](#)]
44. Wang, W.; Chen, X.-Q.; Liu, G.; Shen, Z.; Xia, D.; Wong, P.K.; Yu, J.C. Monoclinic dibismuth tetraoxide: A new visible-light-driven photocatalyst for environmental remediation. *Appl. Catal. B Environ.* **2015**, *176*, 444–453. [[CrossRef](#)]
45. Long, Y.; Li, L.; Wang, S.; Chen, Y.; Wang, L.; Zhang, S.; Luo, L.; Jiang, F. Photocatalytic Removal of 17 α -Ethinyl Estradiol Using the Bi₂O₃/Bi₂O₄ Photocatalyst. *Catal. Lett.* **2018**, *148*, 3608–3617. [[CrossRef](#)]
46. Xia, J.; Ji, M.; Di, J.; Wang, B.; Yin, S.; He, M.; Zhang, Q.; Li, H. Improved photocatalytic activity of few-layer Bi₄O₅I₂ nanosheets induced by efficient charge separation and lower valence position. *J. Alloys Compd.* **2017**, *695*, 922–930. [[CrossRef](#)]

47. Cui, S.; Shan, G.; Zhu, L. Solvothermal synthesis of I-deficient BiOI thin film with distinct photocatalytic activity and durability under simulated sunlight. *Appl. Catal. B Environ.* **2017**, *219*, 249–258. [[CrossRef](#)]
48. Cheng, H.; Huang, B.; Dai, Y.; Qin, X.; Zhang, X. One-Step Synthesis of the Nanostructured AgI/BiOI Composites with Highly Enhanced Visible-Light Photocatalytic Performances. *Langmuir* **2010**, *26*, 6618–6624. [[CrossRef](#)]
49. Wang, Y.; Deng, K.; Zhang, L. Visible Light Photocatalysis of BiOI and Its Photocatalytic Activity Enhancement by in Situ Ionic Liquid Modification. *J. Phys. Chem. C* **2011**, *115*, 14300–14308. [[CrossRef](#)]
50. Ning, S.B.; Lin, H.X.; Tong, Y.C.; Zhang, X.Y.; Lin, Q.Y.; Zhang, Y.Q.; Long, J.L.; Wang, X.X. Dual couples Bi metal depositing and Ag@AgI islanding on BiOI 3D architectures for synergistic bactericidal mechanism of E-coli under visible light. *Appl. Catal. B Environ.* **2017**, *204*, 53–60. [[CrossRef](#)]
51. Chang, C.; Zhu, L.; Fu, Y.; Chu, X. Highly active Bi/BiOI composite synthesized by one-step reaction and its capacity to degrade bisphenol A under simulated solar light irradiation. *Chem. Eng. J.* **2013**, *233*, 305–314. [[CrossRef](#)]
52. Bao, C.; Wang, C.; Fan, D.; Ma, H.; Hu, L.; Fan, Y.; Wei, Q. A novel sandwich-type photoelectrochemical sensor for SCCA detection based on Ag₂S-sensitized BiOI matrix and Au@Pd shell nanoflower label for signal amplification. *New J. Chem.* **2018**, *42*, 15762–15769. [[CrossRef](#)]



© 2019 by the authors. Licensee MDPI, Basel, Switzerland. This article is an open access article distributed under the terms and conditions of the Creative Commons Attribution (CC BY) license (<http://creativecommons.org/licenses/by/4.0/>).